

# Biochemical Characterization of Mouse Retina of an Alzheimer's Disease Model by Raman Spectroscopy

Clara Stiebing,<sup>#</sup> Izabella J. Jahn,<sup>#</sup> Michael Schmitt, Nanda Keijzer, Robert Kleemann, Amanda J. Kiliaan, Wolfgang Drexler, Rainer A. Leitgeb, and Jürgen Popp\*

Cite This: *ACS Chem. Neurosci.* 2020, 11, 3301–3308

Read Online

ACCESS |

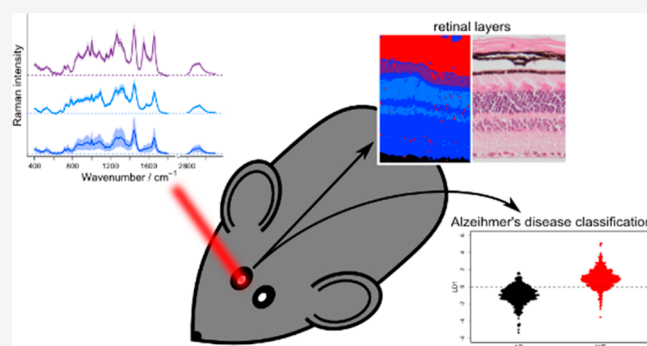
Metrics & More

Article Recommendations

Supporting Information

**ABSTRACT:** The presence of biomarkers characteristic for Alzheimer's disease in the retina is a controversial topic. Raman spectroscopy offers information on the biochemical composition of tissues. Thus, it could give valuable insight into the diagnostic value of retinal analysis. Within the present study, retinas of a double transgenic mouse model, that expresses a chimeric mouse/human amyloid precursor protein and a mutant form of human presenilin 1, and corresponding control group were subjected to *ex vivo* Raman imaging. The Raman data recorded on cross sections of whole eyes highlight the layered structure of the retina in a label-free manner. Based on the Raman information obtained from *en face* mounted retina samples, a discrimination between healthy and Alzheimer's disease retinal tissue can be done with an accuracy of 85.9%. For this a partial least squares-linear discriminant analysis was applied. Therefore, although no macromolecular changes in form of, *i.e.*, amyloid beta plaques, can be noticed based on Raman spectroscopy, subtle biochemical changes happening in the retina could lead to Alzheimer's disease identification.

**KEYWORDS:** retinal layers, Raman imaging, APP/PS1 mouse, Alzheimer's disease, PLS-LDA



investigated sample is subjected to laborious preparation steps, and a frequent concern is the questionable specificity of many of the labels used in these studies.

## INTRODUCTION

One of the most controversial discussion topics on Alzheimer's disease (AD) research is whether specific biomarkers can be detected noninvasively in the retina.<sup>1–3</sup> The eye is part of the cerebral nervous system, and it is the only region that can be imaged *in vivo* noninvasively by optical methods. If the AD pathogenesis would manifest itself in the retina at early stages of the disease and these biochemical changes could be detected, valuable insights that are not accessible at the moment would be gained. Optical coherence tomography (OCT) is the method of choice for performing ophthalmologic investigations *in vivo*. This method gives morphological information on the layered structure of the retina. Based on the OCT images, medical conditions of the eye that involve structural changes of the retinal layers can be diagnosed. However, it is believed that these changes are preceded by subtle biochemical modifications of the retina that cannot be detected by OCT. The identification of the amyloid  $\beta$  plaques and phosphorylated tau tangles in *ex vivo* retina samples has been reported in mouse models<sup>4–7</sup> as well as human eyes.<sup>4,6,8</sup> Nevertheless, there are also studies that report on the absence of these biomarkers at the retina level and question the diagnostic value of this approach.<sup>9–11</sup> The described detection methods are mostly based on labels, such as curcumin, Thioflavin-S, or amyloid  $\beta$  antibody. This requires that the

investigated sample is subjected to laborious preparation steps, and a frequent concern is the questionable specificity of many of the labels used in these studies.

Raman spectroscopy is known to provide label-free molecular specific fingerprint information, and thus, it can monitor subtle biochemical changes on the cellular level. It is often applied to identify pathogens or in imaging applications to detect cancerous tissue sites.<sup>12</sup> Tissue samples can be measured in their native form under *in vivo* or *ex vivo* conditions. In the latter case, snap-frozen thin sections deposited on quartz or CaF<sub>2</sub> slides are preferred. Therefore, elaborate fixation and staining steps are not necessary.

The number of publications focusing on AD biomarker detection via Raman spectroscopy in tissue samples has increased during the last years.<sup>13–19</sup> The focus of most of them lies on the localization of amyloid  $\beta$  plaques in brain tissue of mouse models and AD patients. Palombo *et al.*<sup>13</sup> combined immunofluorescence imaging with Fourier-transform infrared

Received: July 8, 2020

Accepted: September 29, 2020

Published: September 29, 2020



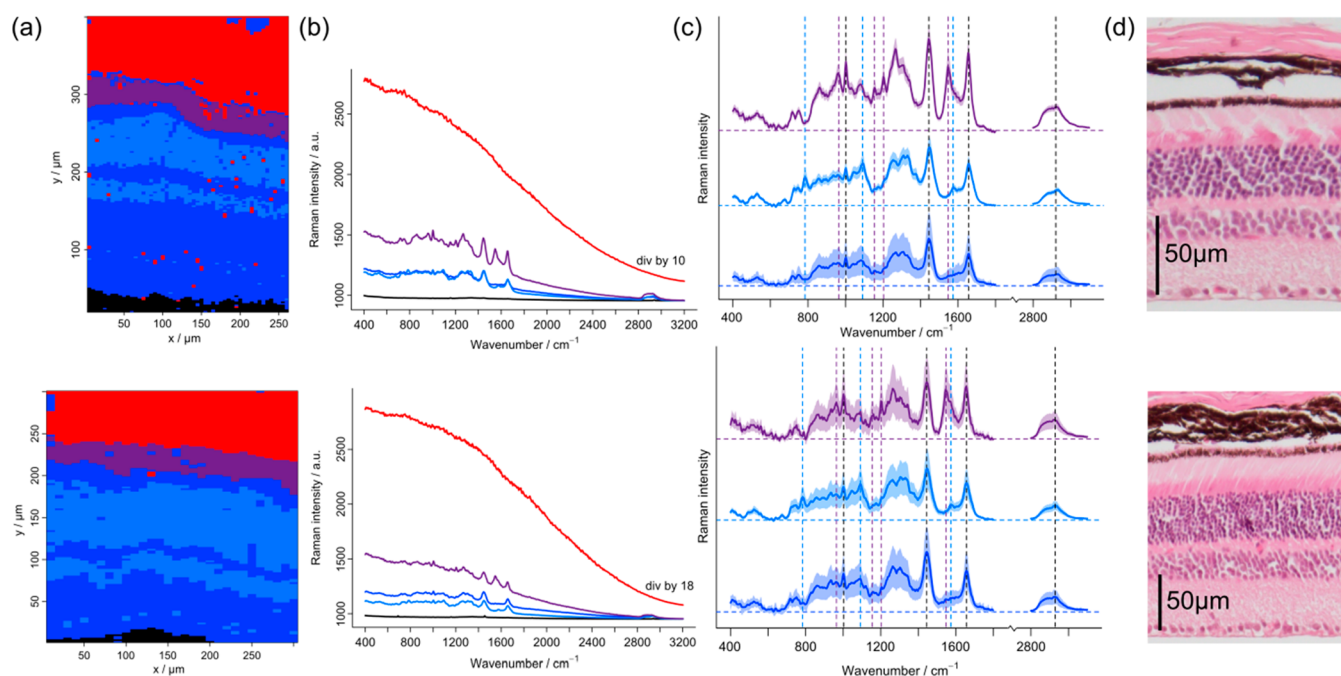


**Figure 1.** Raman-based HCA cluster images (a) of a  $400 \times 260 \mu\text{m}^2$  region ( $2 \mu\text{m} \times 5 \mu\text{m}$  pixel size) of the retina cross section of an AD mouse (top) and a  $300 \times 300 \mu\text{m}^2$  region ( $2 \mu\text{m} \times 10 \mu\text{m}$  pixel size) of the retina cross section of a WT mouse (bottom). The corresponding cluster centroids are depicted as raw mean spectra (b) and background-corrected mean spectra (c) based on the HCA clusters in the same color-coding. H&E-stained retina cross section of an AD (top) and WT (bottom) mouse (d) correlates well to the cluster images in (a).

and Raman spectroscopy and showed that a lipid ring surrounds the protein rich plaques. This was further supported by two other studies based on stimulated Raman scattering microscopy on brain tissue.<sup>16,19</sup> In a recent report, however, Lochocki *et al.*<sup>15</sup> performed Raman imaging on postmortem brain tissue of AD patients and found contradictory results. Autofluorescence images performed prior to Raman measurements of the investigated tissues showed uniformly distributed bright spots that could be falsely associated with amyloid  $\beta$  plaques but could not be confirmed via Thioflavin-S staining. Instead, the bright spots were associated with lipofuscin. Lipofuscin aggregates are formed by lipids, metals, and misfolded proteins, containing fine yellow-brown granules, and are linked with neuronal loss and might have an active role in neurodegeneration.<sup>20</sup> In the Raman maps, these regions showed high fluorescence signals, probably caused by the chromophores present in lipofuscin. A unique plaque-specific spectrum could not be determined even after possible spectral interferences were carefully removed.

The number of reported Raman studies on retina samples is scarce.<sup>21–25</sup> This might be due to the rapid degradation of the retina after death and the challenges associated with *in vivo* Raman measurements on the eye. The studies published by Gellerman *et al.*<sup>25</sup> on the distribution of carotenoid content in the macula via resonance Raman spectroscopy are the only *in vivo* applications reported so far. However, by using resonance Raman spectroscopy, valuable information from a biological material, whose signals are not enhanced, are lost. In a previous publication, we showed that the *ex vivo* human retina delivers very rich spectral information when investigated with an excitation wavelength outside of resonances at 785 nm.<sup>21</sup> Raman imaging provided valuable insights into the molecular composition by probing the entire molecular fingerprint, *i.e.*, the lipid, protein, carotenoid, and nucleic acid content. Furthermore, we also showed that comparable Raman spectra

of isolated human retina can also be obtained under laser safety regulations required for *in vivo* investigations.

So far, no investigations on the potential of Raman spectroscopy to discriminate between healthy and diseased retina samples have been conducted. In the current study, retinas of a double transgenic mouse model (APP/PS1) that expresses a chimeric mouse/human amyloid precursor protein (APP; Mo/HuAPP695swe) and a mutant form of human presenilin 1 (PS1-dE9) were subjected to *ex vivo* Raman imaging. Raman maps of eye cross sections of both wild type (WT; C57BL/6J) and APP/PS1 (AD) mouse model as well as *en face* mounted isolated retinas were measured. We show that this label-free approach provides information on the biochemical composition of the retinal layers and can discriminate between healthy and diseased samples with an accuracy of 86% based on the acquired Raman spectra.

## RESULTS AND DISCUSSION

**Identification of Retinal Layers by Raman Spectroscopy.** To investigate whether the different retinal layers can be discriminated based on distinct Raman signals, cross sections of murine eyes collected from a WT and AD mouse have been subjected to Raman imaging. The retina of vertebrates consists of 10 different layers. In order to capture the layered structure of the retina, a spatial resolution of  $2 \mu\text{m}$  across the layers was used. The inner and outer limiting membranes, however, have a thickness smaller than  $1 \mu\text{m}$ ,<sup>26</sup> and therefore, they cannot be resolved due to the chosen measurement conditions. In Figure 1a, the Raman-based images show several layers highlighted with different colors corresponding to five clusters obtained after hierarchical cluster analysis (HCA), which groups the spectra of the recorded data based on the similarity of their spectral profile. The mean spectra for each cluster (raw and processed) are also shown in the same figure. The black cluster in Figure 1b contains no Raman information as the

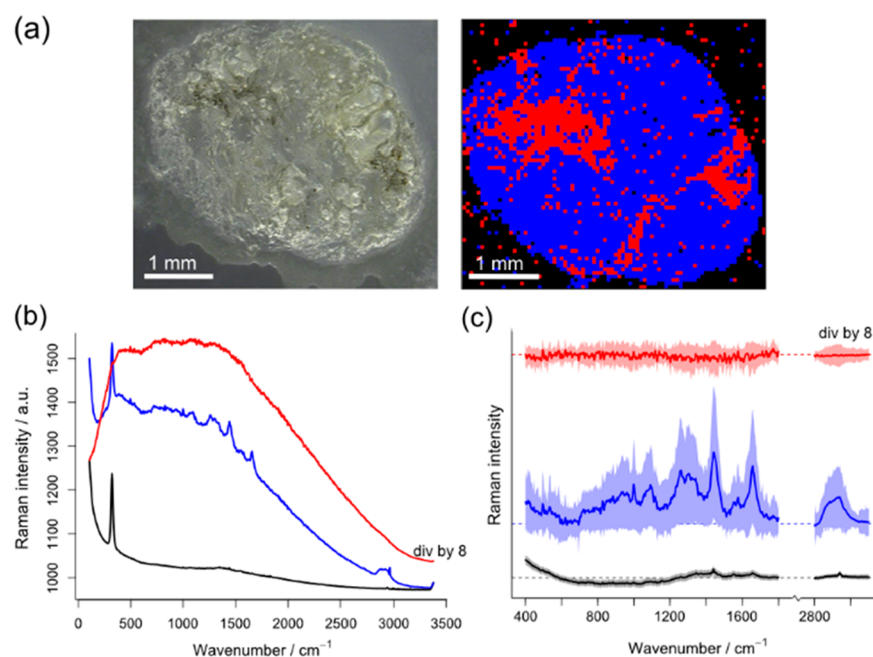


**Figure 2.** Bright field image (left) and Raman-based HCA cluster image (right) depicting a representative *en face* retina (a). Corresponding cluster centroids are displayed as raw mean spectra (b) and background-corrected mean spectra (c) based on HCA clusters of a Raman image in the same color coding. Only spectra from the blue cluster contain retinal Raman information.

measurement positions were situated outside of the tissue. The red cluster is dominated by the fluorescence emission of chromophores, mainly melanin granules, found in the retinal pigment epithelium (RPE) and choroid. Despite of using 785 nm as the excitation wavelength for the Raman scattering, the detection of Raman signals from this region turned out to be challenging. Having in mind the aimed application, *in vivo* Raman spectroscopy on the human retina, two aspects concerning fluorescence generation should be considered. First, the RPE of mice is stronger pigmented than the one of humans. Second, the laser focus will mainly probe the inner layers (close to the vitreous humor) of the retina with a thickness of around 500  $\mu\text{m}$ . Therefore, under *in vivo* measurement conditions, where the human retina is investigated from the front side, it is expected that significantly less fluorescence will be induced and collected from the RPE leading to a significantly reduced background.

An extended multiplicative scatter correction algorithm (EMSC) was used to effectively correct for the varying background contributions within each data set (see [Chemometric Analysis](#)). The background-corrected spectra of the three clusters rich in Raman information are plotted in [Figure 1c](#). Raman bands typically assigned to proteins and lipids can be seen in all three clusters, namely, the C=C stretching mode at 1657  $\text{cm}^{-1}$ , CH<sub>2</sub> bending vibration at 1445  $\text{cm}^{-1}$ , ring breathing mode of phenylalanine at 1003  $\text{cm}^{-1}$ , and CH stretching modes in the high wavenumber region with a maximum at 2933  $\text{cm}^{-1}$ . The purple cluster corresponds to the outer and inner segment containing rods and cones. In the case of nocturnal animals, the photoreceptor cells are rod dominated. Rhodopsin, the main chromophore found in rods, is a light-sensitive receptor protein that enables vision in low-light conditions. The bands at 1548, 1204, 1155, and 965  $\text{cm}^{-1}$  are the most prominent Raman modes associated with N-H bending, C-C, and C=C stretching vibrations of this molecule.<sup>27,28</sup> In the case of the light blue cluster, as

compared to the two other ones, a higher nucleic acid content can be seen due to distinctive bands at 785, 1092, and 1574  $\text{cm}^{-1}$ . The two layers can be assigned to the inner and outer nuclear layer of the retina. Additionally, scattered pixels attributed to the same cluster can be observed in the lower side of the Raman image. This might originate from the ganglion cells that are dispersed over the inner side of the retina and do not form a large distinctive nuclear layer. Lastly, the dark blue cluster can be associated with the inner and outer plexiform layers, where a network of axons and synapses enables communication between cells.

In routine analysis the investigation of the biochemistry of tissue sections, such as retina, is performed via histological analysis. To correlate the Raman cluster images, standard hematoxylin and eosin (H&E) staining was performed on an AD and a WT mouse eye cross section. The resulted micrograph shows also a layered structure of the retina, which corresponds well to the described Raman cluster images (see [Figure 1d](#) and [Figure S1](#) in the [Supporting Information](#)). Staining procedures require elaborate sample preparation steps to be carried out before the actual imaging, and detection of a particular pathogenic factor or a biomarker expressed in a tissue relies on antibodies with high sensitivity and specificity.

Furthermore, a series of stainings and control stainings (in which antibodies are omitted) have to be performed to demonstrate specificity.<sup>7</sup> In the case of Raman imaging, sample preparation only needs cryo-sectioning of the tissue which significantly decreases the possibility of alterations and artifacts caused by sample handling or the detection strategy (e.g., antibody or other labels). Therefore, *ex vivo* Raman investigations of retina samples can be carried out label-free and, in addition, might give significant insights into the biochemical changes of biological tissues.

All investigated retina samples (see [Figure S2](#) in the [Supporting Information](#)) showed the well-known layered structure with some spectral differences due to local

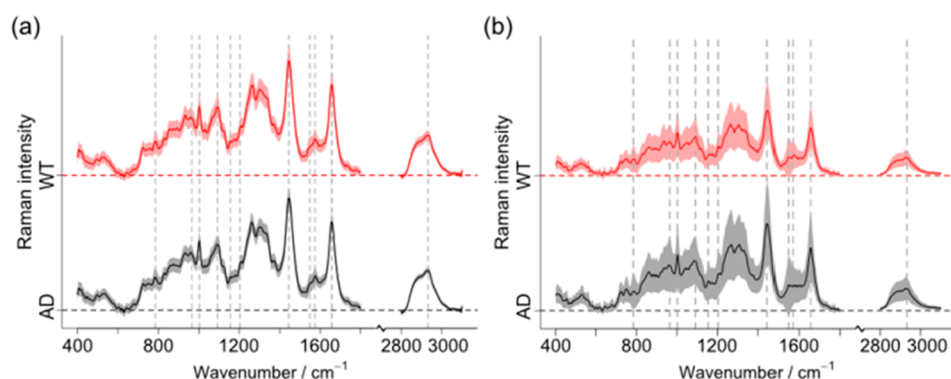


**Figure 3.** Overall mean spectra based on the two groups WT (red) and AD mice (black) of the *en face* Raman measurements used for the classification model (a) and the cross sections (b) shown in Figure 1.

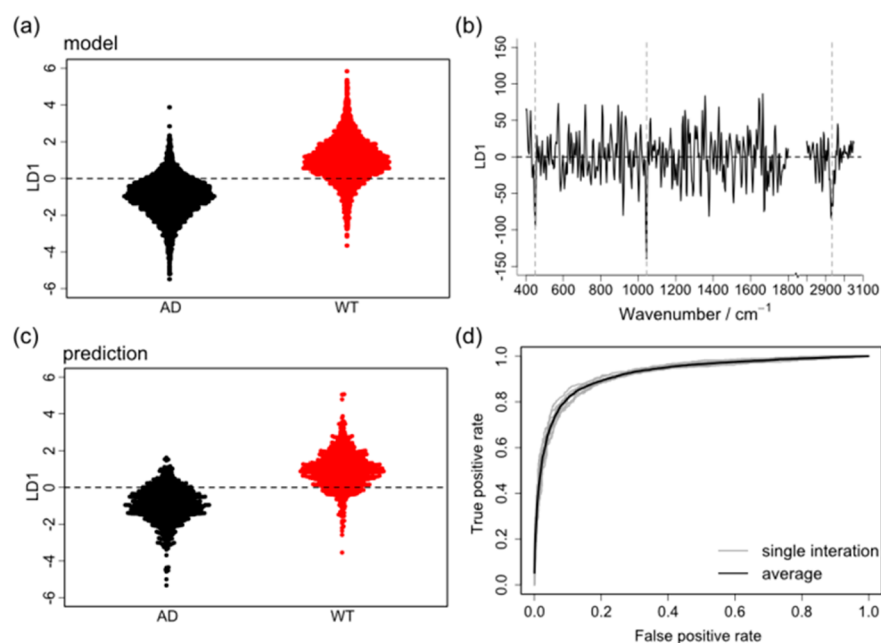


**Figure 4.** Trained PLS-LDA model representing the LD1 coefficients for one iteration based on the two groups (a) and in the spectral domain (b). Prediction of the unknown spectra based on the developed model (c). ROCs of the 10-fold internal cross validation are shown in gray and their average in black (d).

biochemical variations. The HCA analysis did not reveal any in small spots concentrated cluster that could be assigned to extracellular amyloid  $\beta$  aggregates. In order to get a complete picture, Western blots were performed on homogenized retina samples (see Supporting Information for further details) with various amyloid  $\beta$  antibodies. In Figure S3, no differences between WT and AD mice were observed regarding the presence of the amyloid  $\beta$  protein. These findings are supported by a recent study reported by the group of Baumann,<sup>5</sup> where retinas of APP/PS1 mice were subjected to OCT, immunohistochemical staining and fluorescence investigations in order to assess the diagnostic value of retinal analysis for AD. They found that only one mouse out of 17 mice showed fluorescence signals that could be attributed to extracellular amyloid  $\beta$  accumulation located ca. 15  $\mu\text{m}$  below the surface of the retina extending into the inner plexiform layer. This particular mouse was 104 weeks old. Compared to the present study, the Raman images presented in Figure 1 were measured on retinas of 48 week old mice. Hence, the

absence of amyloid  $\beta$  accumulations in the Raman images is in line with the findings of the Baumann group.

**Discrimination of Healthy vs AD Diseased Retina.** As outlined above, the development of mature AD-associated plaques inside the mouse retina especially in early weeks is rather unlikely. However, biochemical changes as precursors of plaque formation might already occur. To investigate the possibility that Raman analyses allow differentiation between retinas from the healthy WT control mice versus AD-prone APP/PS1 mice, *en face* Raman images of the entire retinas were recorded. Instead of probing the different layers in the cross sections, here the information on the inner layers of the retina are gathered at once. The *en face* configuration was chosen because it mimics future *in vivo* experiments and facilitates the translation to settings in patients.

Figure 2a displays a bright field image of a representative *en face* retina (WT) and the resulting Raman-based HCA cluster image. As no macroscopic differences were noticed between the bright field images of the different samples, for clarity just one image is provided. The HCA cluster centroids are plotted

as means without (b) and with the implemented EMSC background correction (c) in the same color coding. The black cluster represents the locations outside the sample and the red cluster corresponds to areas with high fluorescence masking any Raman information. These fluorescent areas are corresponding to dark locations in the bright field image, hinting at high pigmentation, most likely due to remains from the RPE and choroid, which was not fully detached during the isolation. As seen in the red spectra of Figure 2b and c, the fluorescence is effectively filtered out by the EMSC algorithm. Only the blue cluster shows distinct Raman bands containing retinal information.

Each *en face* Raman image was processed using HCA clustering and only spectra containing retinal Raman information (blue cluster) were used to build the following classification model. Figure 3a presents the mean of all spectra used for the classification separated by the two groups; WT control mice (red) and AD mice (black), as outlined under Chemometric Analysis. Typical Raman bands of lipids and proteins at 1003, 1445, and 1657  $\text{cm}^{-1}$  as well as the characteristic CH stretching region at high wavenumbers can be seen in both spectra. Furthermore, bands corresponding to nucleic acids around 785, 1029, and 1574  $\text{cm}^{-1}$  are present, indicating that the Raman focus reached into the nuclear layers of the retinas. Even small contributions of Rhodopsin can be identified at 965, 1155, 1204, and 1548  $\text{cm}^{-1}$ . To allow a comparison between the *en face* and cross section samples, the spectra of the cross section measurements shown in Figure 2c were averaged and are displayed in Figure 3b. The results are in high agreement with each other. The intensity of the Rhodopsin signals is slightly smaller in the *en face* measurements compared to the cross sections. Most likely, the laser focus does not reach the entire rod-containing layer in *en face* mounted samples.

Figure 3a shows that the spectra obtained by *en face* imaging of the retinas from WT reference and AD mice are not distinguishable by naked eye, which is in line with the observed structural similarity of the cross sections of Figure 1. To detect underlying subtle changes in the Raman profiles, a partial least squares-linear discriminant analysis (PLS-LDA) was applied to the data set (see Chemometric Analysis). Figure 4 represents the results of one iteration of the 10-fold internal cross validation. In Figure 4a each spectrum used for building the PLS-LDA model is represented by a dot and grouped into the two classes (AD, black; WT, red). The coefficients plotted as LD1 determine the model-based separation of the two classes (dotted line), which is plotted in Figure 4b in the spectral domain. Negative features (bands) are more pronounced in spectra corresponding to AD, while positive features correspond to the WT group. Hence, bands at 2933, 1045, and 450  $\text{cm}^{-1}$  are more prominent in spectra of AD than of WT and furthermore can be assigned to proteins. This indicates an early stage biochemical change in the protein composition that precedes the more conventional late-stage structural changes and pathological manifestation of AD. For the purpose of testing how well the model performs, the recorded data set was split before modeling. The groups of the unknown spectra were then predicted and the results are shown in Figure 4c. Again a clear separation between the two classes was found as most spectra were grouped in their corresponding classes (AD, 591; WT, 580 correctly classified out of each 693 spectra). In Figure 4d, the receiver operating curve (ROC) is shown for the 10-fold cross validation

including the single iterations in gray and their average in black. Due to only small variations of the ROCs between the single iterations, it can be seen that the model is stable. In total for all iterations, a sensitivity of 86.2% and a specificity of 85.5% were achieved. Hence, a discrimination between healthy and AD diseased retinal tissue with the established model is possible with an accuracy of 85.9%.

## CONCLUSIONS

Raman spectroscopic investigations provided rich information on the biochemistry of mouse retinas without any labeling or sophisticated sample treatment. In an *ex vivo* setting, insight into the layered structure of retina cross sections was provided without the need of staining procedures. The layers were identified based on their different contents of nucleic acids, Rhodopsin, lipids, and proteins. A similar spectral profile is recorded, when investigating *en face* mounted samples: a configuration which is closer to the targeted *in vivo* application. Here, the layers are recorded simultaneously, and the Raman signals are accumulated into one spectrum. With a focus on Alzheimer's disease detection, the Raman signature of retinas of AD-prone APP<sup>swe</sup>/PS 1dE9 mouse model was compared to Raman spectra of retinas of the C57BL/6J wildtype model. Clear amyloid beta accumulations could not be found in either the cross sections or the *en face* samples, which is in line with recently published investigations using modalities such as OCT, fluorescence, and immunohistochemical staining. However, subtle underlying changes in the biochemistry of the retina could be identified by chemometric modeling. With a sensitivity of 86.2%, spectra of AD-diseased mice were correctly recognized as such.

## METHODS

**Materials. Biobank Tissue.** Eye and brain biopsies from a mouse tissue biobank at Radboud University Nijmegen Medical Center (Nijmegen, The Netherlands) were used. The biobank contains tissue from reference control groups and surplus mice of breeding. The animals were subjected to 0.1 M PBS transcardial perfusion. Methodological details of organ collection and processing are provided in the paragraphs below. For the present study, we have used tissues from APP<sup>swe</sup>/PS 1dE9 mice (AD) generated by Jankowsky and Borchelt<sup>29</sup> that were backcrossed on C57BL/6J background as described in detail by Wiesmann *et al.*<sup>30</sup> and respective control tissue from wildtype C57BL/6J mice (WT). The mice brain tissues were characterized for the presence (AD) and absence (WT) of amyloid  $\beta$ 1–42 immunoreactivity as detailed in Supporting Information Figure S4. Biopsies of male and female mice were used for this study, and all tissues were processed at TNO, Leiden, The Netherlands.

**Preparation of Cross Sections of Whole Eyes.** To generate whole eye cross sections for Raman measurements, frozen eyes stored at  $-80\text{ }^{\circ}\text{C}$  were embedded in Tissue Tek (Sakura Finetek Europe b.v., Alphen a/d Rijn, The Netherlands) and 10  $\mu\text{m}$  sagittal slices were made on a Leica CM1950 cryostat at TNO (Leiden, The Netherlands). Four sections from WT and five sections from AD mouse eye were mounted on CaF<sub>2</sub> slides (Crystal GmbH, Berlin, Germany) and shipped frozen on dry ice to Leibniz Institute of Photonic Technology (Leibniz-IPHT) for Raman measurements. The cross sections are from one female AD and one female WT mice with an age of 48 weeks. WT and AD eyes used for whole eye cross sections for histological staining were from male mice with an age of 38 weeks.

**Preparation of En Face Samples.** For *en face* Raman measurements, left and/or right eyes from 10 AD mice and 10 WT mice were used. This allowed isolation of 15 AD and 15 WT retinas suitable for Raman imaging. The age of the mice used for *en face* Raman analyses

was 12 months. Eyes were carefully thawed in 4 °C cold 1× PBS for the duration of 1 h and afterward transferred onto a gauze soaked in cold 1× PBS in a Petri dish. The cornea was removed by an incision at the limbus into the anterior chamber. Scissors were then inserted into the anterior chamber and circumferential cuts were made in the cornea, just anterior to the limbus, to remove the lens and iris. The eye was opened up with four equally spaced cuts from the ciliary body toward the optic nerve head. The vitreous was removed, and the retina was carefully lifted with forceps and placed on CaF<sub>2</sub> slides, on which the retina was immediately frozen using dry ice. The entire isolation procedure took approximately 10 min. Sample remained frozen and were shipped on dry ice to the Leibniz-IPHT in Jena, Germany for Raman analysis.

**Methods. Histological Staining of Tissues to Characterize Tissue Biopsies.** After enucleation, whole eyes were fixated in 10% buffered formalin for 24 h. Hereafter, eyes were transferred to PBS containing NaN<sub>2</sub> (0.02%) and stored at 4 °C until use. Prior to sectioning, the eyes were embedded in paraffin and 5 μm sagittal sections were made for H&E staining. Digital images of H&E stainings were captured using an Olympus BX51 microscope with an Olympus DP74 camera with 20× magnification.

**Raman Spectroscopic Measurements.** After drying under ambient conditions, Raman images of the isolated retina samples (cross section and *en face*) were recorded with a confocal Raman microscope alpha300 R (WITec, Ulm, Germany) equipped with a diode laser providing an excitation wavelength of 785 nm (Toptica Photonics, Gräfelingen, Germany) with a laser power set to 20 mW at the sample plane. A 300 g/mm grating covered the complete wavenumber region from 100 to 3300 cm<sup>-1</sup> with a spectral resolution of around 6 cm<sup>-1</sup>. Raman images of retina cross sections were recorded with 3 s integration time using a 50× Zeiss objective with NA 0.9. Several regions were selected on two cross sections for each mouse type. Across the retinal layers a step size of 2 μm and along the layers a step size of 5 or 10 μm was used (see details in the [Supporting Information](#), Table S1). Raman spectra of *en face* retina samples were recorded with 5 s integration time with a previous 3 s prebleaching time to reduce high fluorescence background occurring at locations in the retina, at which the highly pigmented RPE layer and choroid were not completely separated from the isolated retina. A 10× Olympus objective with NA 0.25 was used, and a step size of 50 or 75 μm, depending on the total sample size, was chosen to image the entire retina.

**Chemometric Analysis.** Data processing was performed in R<sup>31</sup> using hyperSpec<sup>32</sup> as a main package. Preprocessing of the spectra included wavenumber calibration with paracetamol as a reference, a wavenumber interpolation step, background correction using the EMSC, and cosmic spike correction.<sup>33</sup> The EMSC is based on least-squares fitting of single spectra against user-defined spectral profiles including background and pure component spectra, where subsequently the background contributions are subtracted from the raw single spectra. Here, two estimated fluorescence profiles were included as background components, additional to a linear function and an offset. A well-corrected spectrum of an *en face* retina sample was used as a pure component. The wavenumber range from 400 to 3200 cm<sup>-1</sup> was used for analysis. Subsequently, each Raman image was subjected to a HCA algorithm to group the spectra into clusters of the same spectral profile using a Pearson distance calculation and Ward clustering algorithm. The resulting cluster centroids represent weighted average spectra for each cluster and in a false-color representation the spectral differences in the Raman image are visualized. A PLS-LDA was used to build a classification model for the discrimination of healthy (WT) vs AD diseased tissue based on the *en face* retina samples. In total, three batches with each five diseased (AD) and five control (WT) eyes were prepared. Only the spectra of the HCA clusters containing retinal information were included to the model. An area normalization to the high wavenumber region between 2800 and 3100 cm<sup>-1</sup> and a quality control based on a correlation function with a threshold at 0.95 to remove outliers and spectra with low SNR were performed resulting in 6930 AD and 12 253 WT spectra. The reduced number of spectra from the AD

model is for once due to samples being smaller in size and due to a higher amount of fluorescence contribution compared to the WT model. Smoothing of the spectra was performed using a Fourier transformation technique. For modeling, the number of healthy retina spectra was randomly sampled so that the two groups are equal in size. As an external cross validation, the random sampling was performed 10 times. For each iteration, the equalized data set of WT and AD spectra was split in 10 equal folds, where 9 folds were used to train the model and the remaining fold to predict the classes of the spectra. Each fold was once used for prediction. To evaluate the performance of the model, ROCs of the 10-fold iterations were calculated based on the true positive versus the false positive rate by using the R package ROCR.<sup>34</sup>

## ■ ASSOCIATED CONTENT

### Supporting Information

The Supporting Information is available free of charge at <https://pubs.acs.org/doi/10.1021/acschemneuro.0c00420>.

Representative H&E stained eye cross sections of AD and WT control mice; measurement parameters for the cross sections; Raman-based HCA cluster images of retina cross sections; Western blot analysis of retina samples; immunohistochemical analysis of amyloid β (1–42) in brain tissue of AD and WT mice ([PDF](#))

## ■ AUTHOR INFORMATION

### Corresponding Author

Jürgen Popp – Leibniz Institute of Photonic Technology (Leibniz-IPHT), a member of the Leibniz Research Alliance Leibniz Health Technology, 07745 Jena, Germany; Institute of Physical Chemistry and Abbe Center of Photonics, Friedrich Schiller University Jena, 07743 Jena, Germany; [orcid.org/0000-0003-4257-593X](https://orcid.org/0000-0003-4257-593X); Email: [juergen.popp@leibniz-ipht.de](mailto:juergen.popp@leibniz-ipht.de)

### Authors

Clara Stiebing – Leibniz Institute of Photonic Technology (Leibniz-IPHT), a member of the Leibniz Research Alliance Leibniz Health Technology, 07745 Jena, Germany

Izabella J. Jahn – Leibniz Institute of Photonic Technology (Leibniz-IPHT), a member of the Leibniz Research Alliance Leibniz Health Technology, 07745 Jena, Germany; [orcid.org/0000-0002-1186-0925](https://orcid.org/0000-0002-1186-0925)

Michael Schmitt – Institute of Physical Chemistry and Abbe Center of Photonics, Friedrich Schiller University Jena, 07743 Jena, Germany; [orcid.org/0000-0002-3807-3630](https://orcid.org/0000-0002-3807-3630)

Nanda Keijzer – Department of Metabolic Health Research, Netherlands Organisation for Applied Scientific Research (TNO), 2333 CK Leiden, The Netherlands

Robert Kleemann – Department of Metabolic Health Research, Netherlands Organisation for Applied Scientific Research (TNO), 2333 CK Leiden, The Netherlands

Amanda J. Kiliaan – Department of Anatomy Donders Institute for Brain, Cognition, and Behavior Preclinical Imaging Center, Radboud University Medical Center, 6525 EZ Nijmegen, The Netherlands

Wolfgang Drexler – Center for Medical Physics and Biomedical Engineering, Medical University of Vienna, 1090 Vienna, Austria

Rainer A. Leitgeb – Center for Medical Physics and Biomedical Engineering, Medical University of Vienna, 1090 Vienna, Austria

Complete contact information is available at:

<https://pubs.acs.org/10.1021/acscchemneuro.0c00420>

## Author Contributions

#C.S. and I.J. contributed equally.

## Notes

The authors declare no competing financial interest.

## ACKNOWLEDGMENTS

The authors acknowledge financial support from the European Union's Horizon 2020 research and innovation programme (MOON H2020-ICT-2016-1, No 73296).

## REFERENCES

- (1) Ong, S. S., Doraiswamy, P. M., and Lad, E. M. (2018) Controversies and Future Directions of Ocular Biomarkers in Alzheimer Disease. *JAMA Neurol.* 75 (6), 650–651.
- (2) Alber, J., Goldfarb, D., Thompson, L. I., Arthur, E., Hernandez, K., Cheng, D., DeBuc, D. C., Cordeiro, F., Provetti-Cunha, L., den Haan, J., Van Stavern, G. P., Salloway, S. P., Sinoff, S., and Snyder, P. J. (2020) Developing retinal biomarkers for the earliest stages of Alzheimer's disease: What we know, what we don't, and how to move forward. *Alzheimer's Dementia* 16 (1), 229–243.
- (3) Ngolab, J., Honma, P., and Rissman, R. A. (2019) Reflections on the Utility of the Retina as a Biomarker for Alzheimer's Disease: A Literature Review. *Neurol. Ther.* 8 (S2), 57–72.
- (4) Koronyo, Y., Biggs, D., Barron, E., Boyer, D. S., Pearlman, J. A., Au, W. J., Kile, S. J., Blanco, A., Fuchs, D. T., Ashfaq, A., Frautschy, S., Cole, G. M., Miller, C. A., Hinton, D. R., Verdooner, S. R., Black, K. L., and Koronyo-Hamaoui, M. (2017) Retinal amyloid pathology and proof-of-concept imaging trial in Alzheimer's disease. *JCI Insight* 2 (16), e93621.
- (5) Harper, D., Augustin, M., Lichtenegger, A., Gesperger, J., Himmel, T., Muck, M., Merkle, C., Eugui, P., Kummer, S., Wöhrer, A., Glösmann, M., and Baumann, B. (2020) Retinal analysis of a mouse model of Alzheimer's disease with multicontrast optical coherence tomography. *Neurophotonics* 7 (1), 015006.
- (6) Koronyo-Hamaoui, M., Koronyo, Y., Ljubimov, A. V., Miller, C. A., Ko, M. K., Black, K. L., Schwartz, M., and Farkas, D. L. (2011) Identification of amyloid plaques in retinas from Alzheimer's patients and noninvasive in vivo optical imaging of retinal plaques in a mouse model. *NeuroImage* 54 (Suppl 1), S204–17.
- (7) Ning, A., Cui, J., To, E., Ashe, K. H., and Matsubara, J. (2008) Amyloid-beta deposits lead to retinal degeneration in a mouse model of Alzheimer disease. *Invest. Ophthalmol. Visual Sci.* 49 (11), 5136–43.
- (8) Schultz, N., Byman, E., the Netherlands Brain Bank, and Wennstrom, M. (2020) Levels of Retinal Amyloid-beta Correlate with Levels of Retinal IAPP and Hippocampal Amyloid-beta in Neuropathologically Evaluated Individuals. *J. Alzheimer's Dis.* 73 (3), 1201–1209.
- (9) den Haan, J., Morrema, T. H. J., Verbraak, F. D., de Boer, J. F., Scheltens, P., Rozemuller, A. J., Bergen, A. A. B., Bouwman, F. H., and Hoozemans, J. J. (2018) Amyloid-beta and phosphorylated tau in post-mortem Alzheimer's disease retinas. *Acta Neuropathol. Commun.* 6 (1), 147.
- (10) Ho, C. Y., Troncoso, J. C., Knox, D., Stark, W., and Eberhart, C. G. (2014) Beta-amyloid, phospho-tau and alpha-synuclein deposits similar to those in the brain are not identified in the eyes of Alzheimer's and Parkinson's disease patients. *Brain Pathol.* 24 (1), 25–32.
- (11) Schon, C., Hoffmann, N. A., Ochs, S. M., Burgold, S., Filser, S., Steinbach, S., Seeliger, M. W., Arzberger, T., Goedert, M., Kretzschmar, H. A., Schmidt, B., and Herms, J. (2012) Long-term in vivo imaging of fibrillar tau in the retina of P301S transgenic mice. *PLoS One* 7 (12), e35547.
- (12) Krafft, C., Schmitt, M., Schie, I. W., Cialla-May, D., Matthaus, C., Bocklitz, T., and Popp, J. (2017) Label-Free Molecular Imaging of Biological Cells and Tissues by Linear and Nonlinear Raman Spectroscopic Approaches. *Angew. Chem., Int. Ed.* 56 (16), 4392–4430.
- (13) Palombo, F., Tamagnini, F., Jaynes, J. C. G., Mattana, S., Swift, I., Nallala, J., Hancock, J., Brown, J. T., Randall, A. D., and Stone, N. (2018) Detection of Abeta plaque-associated astrogliosis in Alzheimer's disease brain by spectroscopic imaging and immunohistochemistry. *Analyst* 143 (4), 850–857.
- (14) Michael, R., Lenferink, A., Vrensen, G., Gelpi, E., Barraquer, R. I., and Otto, C. (2017) Hyperspectral Raman imaging of neuritic plaques and neurofibrillary tangles in brain tissue from Alzheimer's disease patients. *Sci. Rep.* 7 (1), 15603.
- (15) Lochocki, B., Morrema, T. H. J., Ariese, F., Hoozemans, J. J. M., and de Boer, J. F. (2020) The search for a unique Raman signature of amyloid-beta plaques in human brain tissue from Alzheimer's disease patients. *Analyst* 145 (5), 1724–1736.
- (16) Ji, M., Arbel, M., Zhang, L., Freudiger, C. W., Hou, S. S., Lin, D., Yang, X., Bacskai, B. J., and Xie, X. S. (2018) Label-free imaging of amyloid plaques in Alzheimer's disease with stimulated Raman scattering microscopy. *Sci. Adv.* 4 (11), eaat7715.
- (17) Fonseca, E. A., Lafeta, L., Cunha, R., Miranda, H., Campos, J., Medeiros, H. G., Romano-Silva, M. A., Silva, R. A., Barbosa, A. S., Vieira, R. P., Malard, L. M., and Jorio, A. (2019) A fingerprint of amyloid plaques in a transgenic animal model of Alzheimer's disease obtained by statistical unmixing analysis of hyperspectral Raman data. *Analyst* 144 (23), 7049–7056.
- (18) Chen, P., Shen, A., Zhao, W., Baek, S. J., Yuan, H., and Hu, J. (2009) Raman signature from brain hippocampus could aid Alzheimer's disease diagnosis. *Appl. Opt.* 48 (24), 4743–8.
- (19) Schweikhard, V., Baral, A., Krishnamachari, V., Hay, W. C., and Fuhrmann, M. (2019) Label-free characterization of Amyloid- $\beta$  plaques and associated lipids in brain tissues using stimulated Raman scattering microscopy. *bioRxiv*, October 1, 2019, ver. 1. DOI: 10.1101/789248.
- (20) Moreno-Garcia, A., Kun, A., Calero, O., Medina, M., and Calero, M. (2018) An Overview of the Role of Lipofuscin in Age-Related Neurodegeneration. *Front. Neurosci.* 12, 464.
- (21) Stiebing, C., Schie, I. W., Knorr, F., Schmitt, M., Keijzer, N., Kleemann, R., Jahn, I. J., Jahn, M., Kiliaan, A. J., Ginner, L., Lichtenegger, A., Drexler, W., Leitgeb, R. A., and Popp, J. (2019) Nonresonant Raman spectroscopy of isolated human retina samples complying with laser safety regulations for in vivo measurements. *Neurophotonics* 6 (4), 041106.
- (22) Marro, M., Taubes, A., Abernathy, A., Balint, S., Moreno, B., Sanchez-Dalmau, B., Martinez-Lapiscina, E. H., Amat-Roldan, I., Petrov, D., and Villoslada, P. (2014) Dynamic molecular monitoring of retina inflammation by in vivo Raman spectroscopy coupled with multivariate analysis. *J. Biophotonics* 7 (9), 724–34.
- (23) Wang, Q., Grozdanic, S. D., Harper, M. M., Hamouche, N., Kecova, H., Lazic, T., and Yu, C. (2011) Exploring Raman spectroscopy for the evaluation of glaucomatous retinal changes. *J. Biomed. Opt.* 16 (10), 107006.
- (24) Erckens, R. J., Jongsma, F. H., Wicksted, J. P., Hendrikse, F., March, W. F., and Motamedi, M. (2001) Raman spectroscopy in ophthalmology: from experimental tool to applications in vivo. *Lasers Med. Sci.* 16 (4), 236–52.
- (25) Tanito, M., Obana, A., Gohto, Y., Okazaki, S., Gellermann, W., and Ohira, A. (2012) Macular pigment density changes in Japanese individuals supplemented with lutein or zeaxanthin: quantification via resonance Raman spectrophotometry and autofluorescence imaging. *Jpn. J. Ophthalmol.* 56 (5), 488–96.
- (26) Heegaard, S., Jensen, O. A., and Prause, J. U. (1986) Structure and composition of the inner limiting membrane of the retina. SEM on frozen resin-cracked and enzyme-digested retinas of Macaca mulatta. *Graefes Arch. Clin. Exp. Ophthalmol.* 224 (4), 355–60.
- (27) Lin, S. W., Kochendoerfer, G. G., Carroll, K. S., Wang, D., Mathies, R. A., and Sakmar, T. P. (1998) Mechanisms of spectral tuning in blue cone visual pigments. Visible and raman spectroscopy of blue-shifted rhodopsin mutants. *J. Biol. Chem.* 273 (38), 24583–91.

(28) Palings, I., Pardoën, J. A., van den Berg, E., Winkel, C., Lugtenburg, J., and Mathies, R. A. (1987) Assignment of fingerprint vibrations in the resonance Raman spectra of rhodopsin, isorhodopsin, and bathorhodopsin: implications for chromophore structure and environment. *Biochemistry* 26 (9), 2544–56.

(29) Jankowsky, J. L., Slunt, H. H., Ratovitski, T., Jenkins, N. A., Copeland, N. G., and Borchelt, D. R. (2001) Co-expression of multiple transgenes in mouse CNS: a comparison of strategies. *Biomol. Eng.* 17 (6), 157–65.

(30) Wiesmann, M., Zerbi, V., Jansen, D., Lutjohann, D., Veltien, A., Heerschap, A., and Kiliaan, A. J. (2017) Hypertension, cerebrovascular impairment, and cognitive decline in aged AbetaPP/PS1 mice. *Theranostics* 7 (5), 1277–1289.

(31) R Core Team (2017) *R: A Language and Environment for Statistical Computing*; R Foundation for Statistical Computing, Vienna, Austria.

(32) Beleites, C., and Sergio, V. *hyperSpec: a package to handle hyperspectral data sets in R*, R package ver. 0.99-20180627. <https://hyperspec.r-forge.r-project.org/>

(33) Ryabchykov, O., Bocklitz, T., Ramoji, A., Neugebauer, U., Foerster, M., Kroegel, C., Bauer, M., Kiehntopf, M., and Popp, J. (2016) Automatization of spike correction in Raman spectra of biological samples. *Chemom. Intell. Lab. Syst.* 155, 1–6.

(34) Sing, T., Sander, O., Beerenwinkel, N., and Lengauer, T. (2005) ROCr: visualizing classifier performance in R. *Bioinformatics* 21 (20), 3940–1.